Quantitative image analysis identifies pVHL as a key regulator of microtubule dynamic instability

Claudio R. Thoma,[1] Alexandre Matov,[2] Katrin L. Gutbrodt,[1] Christian R. Hoerner,[1] Zlatko Smole,[1] Wilhelm Krek,[1] and Gaudenz Danuser[2]

[1]Institute of Cell Biology, Swiss Federal Institute of Technology (ETH) Zurich, 8093 Zurich, Switzerland
[2]Department of Cell Biology, The Scripps Research Institute, La Jolla, CA 92037

Von Hippel-Lindau (*VHL*) tumor suppressor gene mutations predispose carriers to kidney cancer. The protein pVHL has been shown to interact with microtubules (MTs), which is critical to cilia maintenance and mitotic spindle orientation. However, the function for pVHL in the regulation of MT dynamics is unknown. We tracked MT growth via the plus end marker EB3 (end-binding protein 3)-GFP and inferred additional parameters of MT dynamics indirectly by spatiotemporal grouping of growth tracks from live cell imaging. Our data establish pVHL as a near-optimal MT-stabilizing protein: it attenuates tubulin turnover, both during MT growth and shrinkage, inhibits catastrophe, and enhances rescue frequencies. These functions are mediated, in part, by inhibition of tubulin guanosine triphosphatase activity in vitro and at MT plus ends and along the MT lattice in vivo. Mutants connected to the VHL cancer syndrome are differentially compromised in these activities. Thus, single cell–level analysis of pVHL MT regulatory function allows new predictions for genotype to phenotype associations that deviate from the coarser clinically defined mutant classifications.

Introduction

Von Hippel-Lindau (VHL) disease is a hereditary cancer syndrome characterized by a spectrum of benign and malignant tumors, including hemangioblastomas, pheochromocytomas, and clear cell renal cell carcinomas (ccRCCs). Patients with VHL disease inherit a faulty allele of the ubiquitously expressed *VHL* tumor suppressor gene, and emergence of pathology in these patients follows the inactivation of the remaining wild-type allele. Biallelic inactivation of the *VHL* gene also occurs frequently (50–75%) in nonhereditary cancers, in particular sporadic ccRCC, the most common form of kidney cancer.

In humans, the *VHL* gene is expressed in long ($pVHL_{30}$) and short ($pVHL_{19}$) isoforms of 30 kD and 19 kD, respectively (generically referred to as pVHL; Iliopoulos et al., 1998). pVHL has been ascribed multiple functions, each possibly linked to tumor suppression (Frew and Krek, 2008). Widely accepted, pVHL acts as part of an E3 ubiquitin ligase that targets hypoxia-inducible factor (HIF) α subunits for polyubiquitylation in an oxygen-dependent manner (Kaelin and Ratcliffe, 2008). In *VHL*-defective cancers, the HIF transcriptional program is uncoupled from changes in oxygen availability, leading to overproduction of HIF target gene products involved in promoting tumor growth. This pVHL function is differentially compromised by *VHL* mutations linked to VHL disease, which causes mutation-specific variations in disease phenotype (Kaelin, 2008). Specifically, disease-associated *VHL* alleles are subdivided into type 1 (low risk of pheochromocytoma) and type 2 (high risk of pheochromocytoma) disease mutations, with type 2 further subdivided into type 2A (low risk of renal cell carcinoma), type 2B (high risk of renal cell carcinoma), and type 2C (pheochromocytoma only). Type 1 disease is associated with large deletions that affect multiple pVHL functions, including the ability

C.R. Thoma and A. Matov contributed equally to this paper.

Correspondence to Gaudenz Danuser: Gaudenz_Danuser@hms.harvard.edu; or Wilhelm Krek: wilhelm.krek@cell.biol.ethz.ch

C.R. Hoerner's present address is European Molecular Biology Laboratory Heidelberg, 69117 Heidelberg, Germany.

C.R. Thoma's present address is Dept. of Medicine, Brigham and Women's Hospital and Dept. of Genetics, Harvard Medical School, 02115 Boston.

G. Danuser's present address is Dept. of Cell Biology, Harvard Medical School, 02115 Boston.

Abbreviations used in this paper: ccRCC, clear cell renal cell carcinoma; DIC, differential interference contrast; HIF, hypoxia-inducible factor; LAP, linear assignment problem; MAP, MT-associated protein; MT, microtubule; shRNA, small hairpin RNA; shRNAmir, microRNA-based shRNA; VHL, von Hippel-Lindau.

The Rockefeller University Press $30.00
J. Cell Biol. Vol. 190 No. 6 991–1003
www.jcb.org/cgi/doi/10.1083/jcb.201006059

to regulate HIF-α. Type 2 disease is almost invariably linked to *VHL* missense mutations. pVHL mutants linked to type 2A and type 2B VHL disease share an inability to properly regulate HIF, albeit to a different degree (Li et al., 2007), implying that these *VHL* mutations quantitatively alter the ability of pVHL to regulate HIF-α. pVHL mutants associated with type 2C disease seem to retain the ability to target HIF for degradation (Hoffman et al., 2001), suggesting that other pVHL functions are affected in this setting. Together, these findings support the view that *VHL* missense mutations impact the integrity of several distinct functions of pVHL, thus modifying the risk of developing the complex pathologies associated with the VHL cancer syndrome. Therefore, it is critically important to determine the degree to which various functions of pVHL are quantitatively altered by different *VHL* mutations.

Among the HIF-independent functions, pVHL has been shown to bind to microtubules (MTs) along the entire lattice and to protect them from disassembly upon treatment of cells with the MT-depolymerizing drug nocodazole (Hergovich et al., 2003). This function, which appears to be independent of E3 ubiquitin ligase activity, is compromised by type 2A but not type 2B *VHL* mutations. The significance of pVHL's role as an MT-associated protein (MAP) derives from the observation that pVHL is important for primary cilia maintenance and protection from kidney cyst formation, in part by stabilizing MTs or orienting MT growth (Schermer et al., 2006; Thoma et al., 2007; Frew et al., 2008), as well as for the suppression of spindle misorientation (Thoma et al., 2009). This implies that pVHL's tumor suppressor function is licensed, at least in part, through interactions with MTs. Although these qualitative linkages between pVHL and MTs are intriguing, it remains unknown which aspects of MT regulation are affected by *VHL* disease mutants and whether there are quantitative differences among mutants. Such information is indispensable for understanding the molecular basis of the differential risks of kidney cancer linked to distinct *VHL* mutations.

At steady-state, MTs continually switch between phases of growth and shrinkage, a phenomenon known as dynamic instability (Mitchison and Kirschner, 1984). Transitions from growth to shrinkage are referred to as catastrophe events, and transitions from shrinkage to growth are referred to as rescue events. High-resolution measurements of MT length trajectories both in vitro and in vivo have also indicated that growth and shrinkage phases are intermitted by pauses (Keller et al., 2007). Dynamic instability is generally associated with the variable state of GTP nucleotides bound to the tubulin dimers in the MT lattice (Weisenberg et al., 1976). Growing MTs are thought to have at their tip a cap of two to three layers of GTP-tubulin that stabilizes the polymer and increases the affinity for additional GTP-tubulin assembly (Mitchison and Kirschner, 1984; Schek et al., 2007). Catastrophe events may be induced when GTP hydrolysis is temporarily higher than the rate of dimer addition, resulting in abrogation of the stabilizing GTP cap. Evidence suggests that during polymerization, GTP hydrolysis is incomplete, producing GTP remnants along the MT polymer that may facilitate rescue events (Dimitrov et al., 2008). This hypothesis is intriguing as it proposes a mechanism by which MAPs may equally alter the frequencies of catastrophe and rescue by shifting the rate of GTP hydrolysis along the MT lattice and at the cap.

To examine pVHL's regulatory functions as a MAP and to test whether phenotypic variation at the level of the cancer syndrome associated with different *VHL* point mutations would correlate with phenotypic variation at the level of MT dynamics, we computationally tracked a large number of MT growth events in high-resolution live cell images via the plus end marker EB3 (end-binding protein 3)-GFP. We then applied a recently developed method for spatiotemporal grouping of growth tracks to extract additional parameters of MT dynamic instability. Our results suggest that pVHL is a near-optimal MT-stabilizing protein in that it lowers MT turnover and enhances MT stability by reducing catastrophe and increasing rescue frequencies. We mechanistically link these functions of pVHL to the inhibition of tubulin GTPase activity in vitro and in vivo and demonstrate that they are subject to specific alterations by disease-causing *VHL* mutations. Thus, quantitative differences between distinct pVHL mutants with respect to MT dynamic instability regulation may translate into different risks of renal carcinoma in humans.

Results

Automated tracking of MT growth using the plus end marker EB3 establishes pVHL as an attenuator of MT growth

To systematically manipulate the conditions of pVHL expression, we used retinal pigment epithelial (RPE-1) cells and knocked down endogenous levels of wild-type pVHL by transfection of silencing microRNA-based small hairpin RNA (shRNA [shRNAmir]; Fig. 1 A). Conversely, renal cell carcinoma (RCC-4) cells deficient for pVHL were engineered to stably produce either long or short pVHL isoforms (pCMV(R)-VHL_{30} and pCMV(R)-VHL_{19}, respectively; Iliopoulos et al., 1998) or the empty vector as control (pCMV(R)-$VHL^{-/-}$; Fig. 1 B). The same cell system was used to investigate the specific effects on MT dynamics of naturally occurring point mutants of pVHL.

Following our previous observations that pVHL protects MTs from nocodazole-induced depolymerization (Hergovich et al., 2003), we first tested whether the presence and absence of pVHL have a global effect on the density of MTs. Indeed, the normalized immunofluorescence of MTs was increased by ∼40% after reconstitution of wild-type $pVHL_{30}$ in VHL-deficient RCC-4 cells (Fig. 1, C and D), suggesting that pVHL stabilizes MTs. However, the effect was relatively mild ($P < 0.02$). Thus, we suspected that the roles ascribed to pVHL in several MT-dependent cell functions would be more related to its effects on parameters of MT dynamic instability.

MT dynamic instability is an intrinsically stochastic process. Therefore, distributions with hundreds to thousands of values have to be sampled to permit undistorted and significant comparisons between MT behaviors in the presence or absence of pVHL or in association with the expression of different mutants (Jaqaman et al., 2006). To collect unbiased statistics of the dynamics of many MTs, we expressed in both RPE-1 and RCC-4 cells a GFP fusion construct of EB3 and applied a recently developed method for the detection and tracking of EB3-GFP comets (Fig. 1 E and

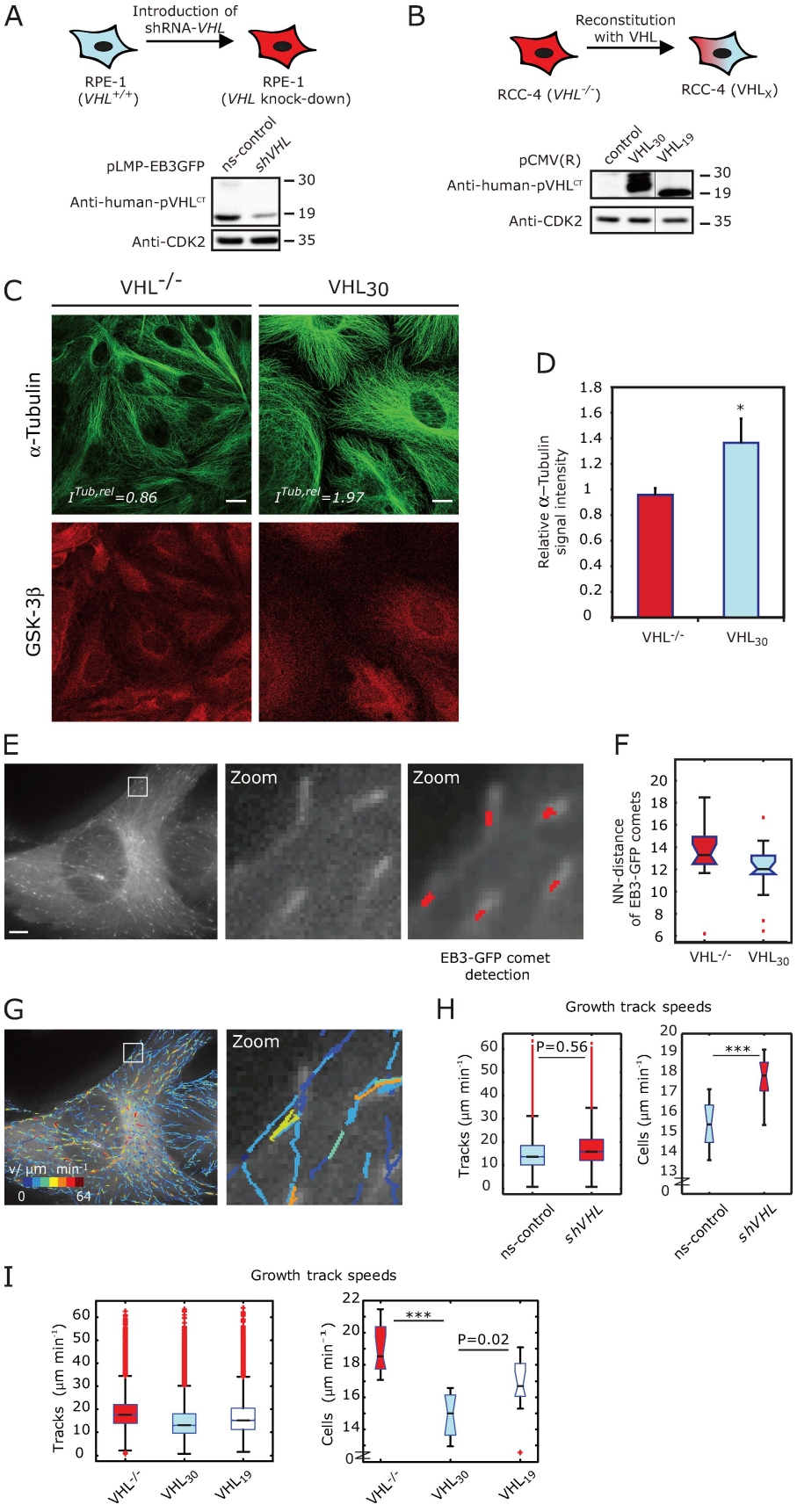

Figure 1. **pVHL attenuates MT growth rate.** (A) RPE-1 cell system and depletion of pVHL using retroviral expression (pLMP-EB3GFP) of shRNAmir against VHL (*shVHL*) and a non-silencing control (ns-control). (B) RCC-4 cell system lacking pVHL expression reconstituted with retroviral expression (pCMV(R)) of the wild-type long form $pVHL_{30}$, the wild-type short form $pVHL_{19}$, and the empty vector as control ($VHL^{-/-}$). Vertical black lines indicate that intervening lanes have been spliced out. (A and B) Molecular mass is indicated in kilodaltons. (C) Immunofluorescence analysis of MT mass in RCC-4 cells expressing the wild-type long form $pVHL_{30}$ or the empty vector ($VHL^{-/-}$). $I^{Tub,rel}$ indicates the α-tubulin signal intensity normalized to GSK-3β signal. (D) Relative α-tubulin signal as measured in C. Data were pooled from $n = 3$ slides, each slide with 10 stacks of five frames each per condition. Mean ± SD is shown (*, $P < 0.02$). (E) Single frame of a video acquired from RPE-1 cells expressing EB3-GFP. Red marks indicate automatic detection of EB3-GFP comets. (F) Mean nearest neighbor distance between EB3-GFP comets in RCC-4 cells ($n = 15$) expressing $pVHL_{30}$ or the empty vector ($VHL^{-/-}$). Box plot indicates distribution of $n = 15$ cells. (G) Overlay to frame in E of EB3-GFP tracks over 125 frames sampled at 0.5 s/frame. Track color encodes speed. (E and G) Zoom panels represent enlargements of the boxed areas in the left panels. (H) Distributions of growth speed of >55,000 tracked EB3-GFP comets in 12 RPE-1 cells (left) and of per cell means (right). Comparison of growth speed distributions was based on Kolmogorov-Smirnov test, and comparison of per cell means was based on the Student's *t* test after validation of normality (***, $P < 10^{-5}$; see Materials and methods). (I) Distributions of growth speed of all tracked EB3-GFP comets (left) and of per cell means (right) in RCC-4 cells (***, $P < 10^{-5}$). See legend for H for statistical test procedures. (F, H, and I) Boxes indicate 25, 50 (median), and 75% quantiles; whiskers extend to 1.5× the interquartile range; red dots indicate outliers beyond this range. Notched boxes indicate uncertainty of the median. Boxes whose notches do not overlap indicate that the medians of the two clusters differ at the 5% significance level. Bars: (C) 10 µm; (E and G) 5 µm.

Videos 1 and 2; Matov et al., 2010). For each condition, 12–15 videos of 125 frames were acquired in three independent sessions at 2-Hz frame rate. EB3 transiently binds to growing MT plus ends (Stepanova et al., 2003), generating a punctuate pattern of EB3-GFP comets throughout the cell. Each video contained ∼30,000–40,000 detectable comets, from which >500 informative MT growth tracks with a lifetime of more than three frames were extracted. Tracks existing for three frames or less had a significant probability of representing random connections between false detection positives. In agreement with the overall slightly higher density of MTs in VHL-expressing cells as compared with cells without pVHL, we found that upon reconstitution of wild-type $pVHL_{30}$ in VHL-deficient RCC-4 cells, the density of EB3 comets was slightly increased, as observed by a reduction of the mean nearest neighbor distance between comets (Fig. 1 F). Again, the statistical significance of this effect was weak (P = 0.11), indicating that effects of pVHL on the overall MT mass and on the density of growing MT ends are minor.

The measured MT growth track speeds (mean velocity over the duration of a track) varied remarkably (Fig. 1, G and H). In RPE-1 cells, the 25% and 75% quartiles were at 10.1 µm min^{-1} and 18.6 µm min^{-1}, respectively, and ∼6% of the tracks reached values 30–60 µm min^{-1}. Validation of these tracks by visual inspection suggested that some of them were caused by erroneous frame to frame links between detected particles and thus outliers to the speed distribution. However, because of the large pool of speed measurements, the low percentage of data outliers had no marked effect on the comparison of MT growth track speeds between different experimental conditions. Depletion of pVHL in RPE-1 cells did not significantly alter the shape of growth track speed distribution (P = 0.56, Kolmogorov-Smirnov test). However, the mean growth speed increased significantly from 15.4 ± 1.1 to 17.8 ± 1.0 µm min^{-1} (mean ± SD of cell to cell variation; $n = 13$). These results indicated that pVHL dampens MT growth overall without differentially affecting the heterogeneous behaviors of MTs throughout the cell.

We first validated this finding by manual tracking of 20 MTs in RPE-1 cells stably expressing GFP-tubulin (Fig. S1, A–E; and Table S1). Second, we repeated our analysis in RPE-1 cells without and with knockdown of pVHL expression based on GFP-CLIP170, an alternative marker of growing MT plus ends (Fig. S1, F and G; Perez et al., 1999). Both experiments confirmed the broad range of MT growth rates but underlined the function of pVHL as attenuator of MT growth. Third, we sought to substantiate this role of pVHL by comparing *VHL*-deficient RCC-4 cells with those producing $pVHL_{30}$ or $pVHL_{19}$ (Fig. 1 I). Interestingly, although both isoforms reduced the growth speed, $pVHL_{19}$ yielded a significantly milder effect than $pVHL_{30}$, suggesting that pVHL interferes with the recruitment and/or incorporation of tubulin dimers to the MT plus end in an isoform-specific manner.

Geometric grouping of growth tracks allows extraction of additional parameters of MT dynamics and reveals pVHL as an attenuator of MT shrinkage

There are several mechanisms by which pVHL may reduce the rate of tubulin addition to the plus end. For example, the presence of pVHL at the MT tip may sterically interfere with dimer-recruiting factors. Alternatively, pVHL may bind to tubulin dimers and thus slow down the incorporation. The latter scenario would cause pVHL to affect only the growth rate, whereas the former would likely be coupled to pVHL-mediated changes in other parameters of MT dynamic instability. Therefore, MT dynamics had to be characterized beyond the instantaneous growth speeds reported by EB3-GFP particles. EB3-GFP particles disappear from the image when the MT switches from a state of growth into a state of shrinkage, i.e., undergoes a catastrophe. They also disappear during MT pauses that last longer than the time it takes EB3 aggregates to dissociate from the tip or because the growing MT tip moves out of focus. In the scenario of a pause, the EB3-GFP particle may reappear near the site of disappearance, indicating the reinitiation of MT growth after pausing. In the scenario of out of focus movement, the particle may reappear in the flight of the terminated track. In both scenarios, the new track has a high probability of being collinear with the terminated track. In the scenario of a track termination caused by catastrophe, a new track may be observed if the shrinking MT is later rescued. The site of track reinitiation has a high probability of being located near the axis of the terminated track in the direction opposite to the previous particle motion.

Accounting for the different scenarios of particle appearances, we spatially and temporally grouped tracks that belonged to the same MT with a high probability (Fig. 2 A and Fig. S3). About 70% of the growth tracks participated in multitrack trajectories that linked visible EB3 growth tracks with forward and/or reverse gaps (Fig. 2 B and Videos 3 and 4). The validity of this approach has been established previously using multispectral live cell images of EB3 comets and tubulin-labeled MTs (Matov et al., 2010). Excellent agreement was found between hand-tracked and computationally tracked growth and shrinkage speeds. In the present study, we repeated the validation by comparing manually tracked MT ends in RPE-1 cells expressing GFP-tubulin with computer-generated growth and shrinkage speeds in EB3-GFP–expressing RPE-1 cells (Tables S1 and S2). Although the data show again good agreement between the shrinkage speeds, the computer-tracked growth speeds are faster. This is caused by regional effects. MTs at the cell periphery, where manual tracking of continuously stained MTs is possible, tend to grow slower than MTs in the perinuclear area (Matov et al., 2010). Direct comparison of the durations of growth, shrinkage, and pause phases is not possible. In trajectories of continuously stained MTs, the transitions between these phases are defined by arbitrary speed thresholds distinguishing growth and shrinkage from pausing. In multitrack trajectories of EB3 comets, the transition between these phases is defined by the disappearance and reappearance of detectable particles. Nevertheless, in Matov et al. (2010), it was established that qualitative changes in these parameters between different experimental conditions are reflected equally by both measurement approaches. This was confirmed in the present study using RPE-1 cells. With silencing VHL, the pause times decreased and the shrinkage times increased, both with manual and computational tracking, whereas growth times remained unchanged (Fig. S1 E and Tables S1 and S2).

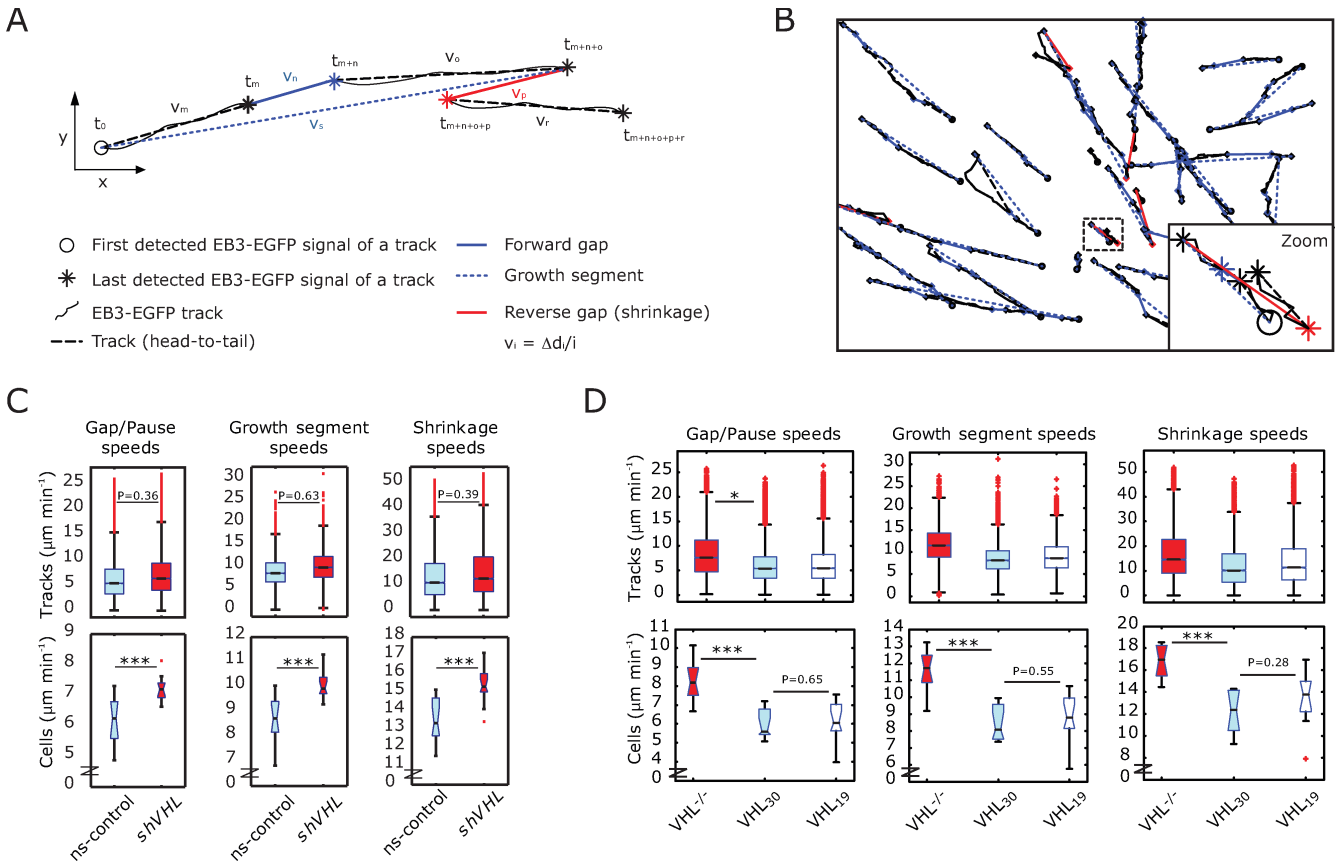

Figure 2. **Clustering of EB3-GFP growth tracks reveals pVHL's function as an attenuator of MT shrinkage rate.** (A) Clustered EB3-GFP tracks with corresponding head to tail tracks, forward gap closure (gap/pause event), and reverse gap closure (shrinkage event) are shown. A series of tracks and forward gap closures not interrupted by a reverse gap closure is referred to as a growth segment. A circle shows the first detected EB3-GFP signal of a track, and asterisks define the last signal of a track in the corresponding color. Growth track speeds (v_m, v_o, and v_r) are defined as the head to tail distance of the track divided by its lifetime (m, o, and r frames, respectively); gap/pause speed (v_n) is defined as the distance between the termination point and the initiation point of the two linked growth tracks divided by the forward gap duration (n frames); accordingly, growth segment speed (v_s) is defined by the distance of the entire growth segment divided by the sum of lifetimes of all included growth tracks and forward gap closures (m + n + o frames); shrinkage speed (v_p) is defined as the distance between the termination point and the initiation point of the two linked growth tracks divided by the reverse gap duration (p frames). (B) Example of clustered growth tracks in a video acquired from RPE-1 cells. Color codes as in A. (C) Analysis of MT dynamics in *n* = 12 RPE-1 cells (Fig. 1 A). Distributions of gap/pause speeds of >23,000 forward gap closures (top) and of per cell mean (bottom), distributions of growth segment speeds of >14,000 growth segments (top) and of per cell mean (bottom), and distributions of shrinkage speeds of >10,000 reverse gap closures and per cell mean are shown (***, $P < 10^{-5}$). (D) Analysis of MT dynamics in *n* = 10 RCC-4 cells (Fig. 1 B). Distributions of MT gap/ pause speeds of >12,000 forward gap closures (top) and of per cell mean (bottom), distributions of growth segment speeds of >8,000 growth segments (top) and of per cell mean (bottom), and distributions of shrinkage speeds of >5,000 reverse gap closures and per cell mean from 10 cells are shown (*, $P < 5 \times 10^{-2}$; ***, $P < 10^{-5}$). (C and D) Boxes indicate 25, 50 (median), and 75% quantiles; whiskers extend to 1.5× the interquartile range; red dots indicate outliers beyond this range. Notched boxes indicate uncertainty of the median. Boxes whose notches do not overlap indicate that the medians of the two clusters differ at the 5% significance level. See Materials and methods for statistical test procedures.

We first examined the effect of pVHL on the gap/pause speed, the growth segment speed, and the shrinkage speed (Table S2). The gap/pause speed is defined by the distance between the sites of termination and reinitiation of two growth tracks connected in forward direction divided by the time elapsed without an EB3 particle (Fig. 2 A). Although the gap/pause speeds were substantially lower than growth track speeds, they were different from zero. Analysis of the speed distributions showed that <15% were >10.1 µm min^{-1}, i.e., the 25–100% range of the growth track speed distribution. This minority of forward gaps was likely to represent temporary out of focus movements, whereas the majority of gaps corresponded to bona fide pauses. The nonzero speed of these gaps originates in the latency of formation of a detectable EB3-GFP particle after growth of a pausing MT is resumed. The mean latency could be estimated as $\Delta\bar{t}_{lat} = \Delta\bar{t}_{gap} \times \bar{v}_{gap} / \bar{v}_{growth}$, i.e., 2.3 s and 2.2 s for RPE-1 cells without and with depletion of pVHL, respectively. The result that these two numbers are statistically indistinguishable for conditions with and without pVHL suggests that pVHL does not significantly interfere with the formation of EB3 particles. This conclusion was further confirmed by colocalization analysis of EB3 comets and pVHL, indicating that pVHL does not preferentially overlap with growing MT ends (Fig. S2).

The growth segment speed is defined by the distance between the site of initiation of the first growth track and the site of termination of the last growth track in a sequence of multiple growth tracks linked by forward gaps only, divided by the time elapsed between the initiation and termination event (Fig. 2 A). The shrinkage speed is defined by the distance between the sites of termination and reinitiation of two growth tracks connected in backward direction divided by the time elapsed without an EB3 particle (Fig. 2 A). Because of the latency in the EB3

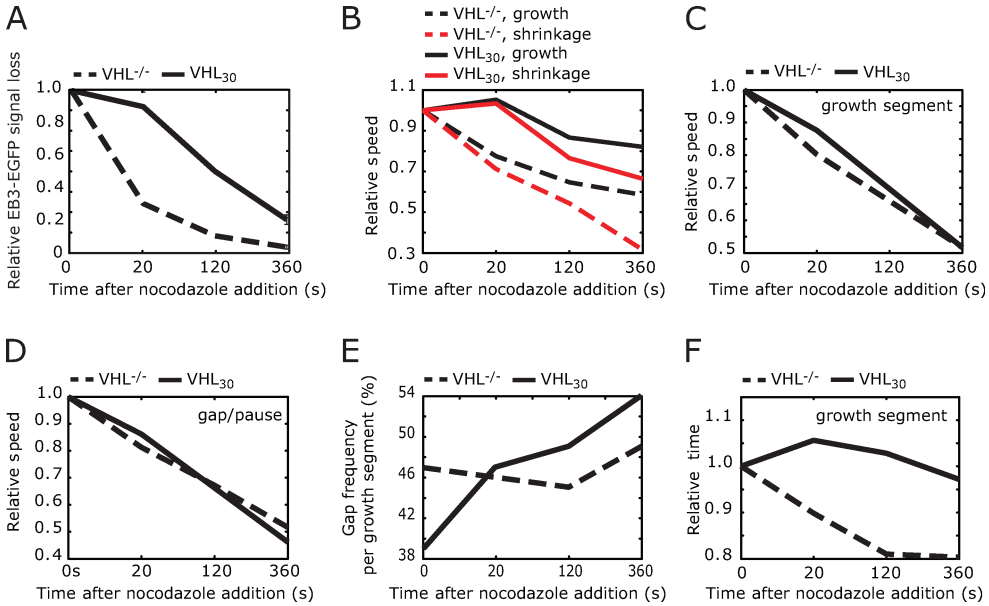

Figure 3. **pVHL enhances MT growth recovery under nocodazole challenge.** (A) Relative loss of EB3-GFP signal after the addition of 40 nM nocodazole to RCC-4 cells reconstituted with the empty retroviral expression vector pCMV(R) ($VHL^{-/-}$) or with pCMV(R) expressing wild-type pVHL (VHL_{30}). (B) Relative slowdown of growth and shrinkage speeds. (C) Relative slowdown of growth segment speeds. (D) Relative slowdown of gap/pause speeds. (E) Change in the frequency of gaps. (F) Relative change in the duration of segments.

particle formation as well as the possibility that the MT pauses throughout the shrinkage phase, the shrinkage speed extracted from linking growth tracks tends to underestimate the instantaneous rate of disassembly of MTs. Nevertheless, significant changes in the characteristics of MT disassembly between different conditions will be detected by this parameter (Matov et al., 2010).

As shown in Fig. 2 C, although the shape of the distributions of gap/pause speed, growth segment speed, and shrinkage speed showed again no differences (top), depletion of pVHL in RPE-1 cells caused an increase in the mean of all three speeds (bottom). Thus, these data confirm pVHL's role as an attenuator of MT assembly and suggest that pVHL also lowers the rate of subunit dissociation during shrinkage. This supports a model in which pVHL is active at the MT tip and along the lattice as opposed to the free tubulin dimer. In agreement with our findings in RPE-1 cells, reconstitution of the long and the short isoforms of pVHL in *VHL*-negative RCC-4 cells attenuated all three additional speed parameters (Fig. 2 D). Interestingly, even though we found isoform-specific attenuation of the growth track speeds (Fig. 1 G), the growth segment speeds of $pVHL_{19}$ and $pVHL_{30}$ did not differ (Fig. 2 D). This adjustment was not caused by a difference in the gap/pause speeds (Fig. 2 D) but was related to prolonged pauses and shortened growth phases of MTs in cells expressing the short isoform (Table S3). Thus, although both isoforms attenuated the growth and shrinkage speeds of MTs, we found that the short isoform was less efficient in attenuation but inhibited more strongly the reinitiation of MT growth after pauses. This notion is further supported by the fact that >40% of all growth segments in cells expressing the long isoform were composed of at least three growth tracks, i.e., had two or more growth reinitiations after pausing, whereas 60% reinitiated growth only once. When expressing the short isoform, this ratio dropped to 30:70.

Acute perturbation of MT polymerization dynamics by nocodazole reveals the inhibition of MT catastrophe and the promotion of rescue as two additional functions of pVHL

To elucidate in more mechanistic terms the finding of pVHL-mediated protection of MTs from nocodazole-induced depolymerization (Hergovich et al., 2003), we treated RCC-4 cells with substoichiometric concentrations of nocodazole (40 nM) and measured over 6 min after perfusion the transient effects on EB3-GFP particle dynamics (Table S4). As expected, nocodazole caused increased particle disappearance over time, yet cells with reconstituted $pVHL_{30}$ expression exhibited a lower decay in particle number (Fig. 3 A and Video 5). Consistent with data from hand-measured, continuously labeled MTs (Vasquez et al., 1997), EB3 particles reported gradual slowing after nocodazole treatment of both growth speeds, as measured by track velocities, and shrinkage speeds, as inferred from the distance and duration of reverse gaps (Fig. 3 B). The decrease of both speeds was suppressed by the expression of $pVHL_{30}$. Although it cannot be ruled out that $pVHL_{30}$ interferes with the binding of nocodazole to tubulin dimers, these data favor a model in which $pVHL_{30}$ weakens interactions between nocodazole and the MT end (Vasquez et al., 1997). Surprisingly, expression of $pVHL_{30}$ had no effect on the speed reduction of either segments or forward gaps (Fig. 3, C and D). Given the differential decrease in track speeds, this suggested differential pausing behaviors of MTs under the challenge of nocodazole in the absence and presence of $pVHL_{30}$. Indeed, we found that the fraction of growth segment time spent in forward gaps increased in the presence of $pVHL_{30}$, whereas it remained unaffected in the absence of $pVHL_{30}$ (Fig. 3 E). At the same time, the duration of growth segments significantly decreased in the absence of $pVHL_{30}$, whereas segment duration

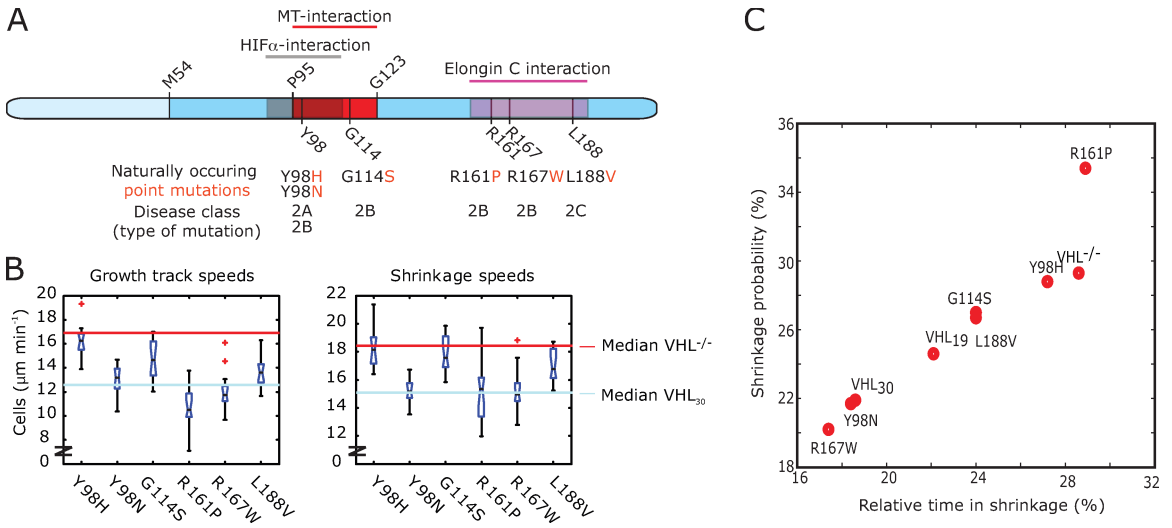

Figure 4. **Analysis of naturally occurring pVHL point mutants.** (A) Position of each naturally occurring point mutation within $pVHL_{30}$ domains and its disease class. $pVHL_{19}$ results from an internal translational initiation site at methionine 54 (M54). (B) Distributions of per cell means of growth track and shrinkage speeds (10–15 RCC-4 cells per mutant). The light blue line indicates the median value of RCC-4 cells expressing wild-type $pVHL_{30}$, and the red line indicates the median value of RCC-4 cells expressing the control vector (Figs. 1 I and 2 D). The speeds distributions of individual MT growth and shrinkage events are presented in Fig. S4 B. Boxes indicate 25, 50 (median), and 75% quantiles; whiskers extend to 1.5× the interquartile range; red dots indicate outliers beyond this range. Notched boxes indicate uncertainty of the median. Boxes whose notches do not overlap indicate that the medians of the two clusters differ at the 5% significance level. (C) Scatter plot of shrinkage probability (probability of a switch from a growth to a shrinkage event) versus time spent in shrinkage, relative to the total duration of trajectories.

stayed almost constant for the period of 6 min in the presence of $pVHL_{30}$ (Fig. 3 F). Together, these data suggest that under the challenge of nocodazole, MTs in *VHL*-deficient RCC-4 cells increasingly underwent catastrophe. Reconstitution of VHL_{30} stabilized these events in pauses from which MT growth could be recovered. Thus, we conclude that besides attenuation of tubulin turnover at the MT end, VHL_{30} takes a second set of roles as a catastrophe inhibitor and rescue factor.

Naturally occurring point mutants with different disease phenotypes exhibit differential defects in attenuating tubulin turnover at growing and shrinking MT ends

To further investigate the dualism of pVHL function in controlling MT dynamics in the context of the VHL cancer syndrome, we generated a panel of RCC-4 cell lines, each producing a different naturally occurring point mutant of $pVHL_{30}$ that is associated with a distinct VHL disease phenotype, including types 2A, 2B, and 2C (Fig. 4 A and Table S5). We hypothesized that this disease-based classification may have a correlate in differential impairments of the two MT-related functions of pVHL. Immunoblotting for pVHL revealed that each mutant protein is produced, albeit at slightly different amounts (Fig. S4 A). This is not unexpected given the different inherited protein stabilities associated with these mutations (Knauth et al., 2006, 2009). As shown in Fig. 4 B, the type 2A mutant $pVHL_{30}$(Y98H) was dysfunctional in attenuating growth and shrinkage speeds, whereas the corresponding type 2B mutant $pVHL_{30}$(Y98N) displayed wild-type behavior with respect to reducing tubulin turnover at the MT ends. Interestingly, another type 2B mutant, $pVHL_{30}$(G114S), was impaired in attenuation of tubulin turnover, as seen by elevated growth track and shrinkage speeds. However, the growth segment speed produced by this mutant was at the level of the growth segment speeds measured in RCC-4 cells expressing $pVHL_{30}$(wt) (Table S5). Thus, similar to the short isoform $pVHL_{19}$(wt), the type 2B mutant $pVHL_{30}$(G114S) affected the instantaneous MT growth but produced globally equal growth rates because MTs spent less time growing and more time pausing (Table S5), which is distinct from type 2B mutant Y98N. Furthermore, like the short isoform, the $pVHL_{30}$(G114S) mutant induced intermediate attenuation of MT shrinkage between complete loss of pVHL function and wild-type behavior (Fig. 4 B). These results suggest that defects in pVHL's MT regulatory functions are not solely associated with type 2A but also with certain type 2B mutants, however with intermediate effects.

Catastrophe inhibition and rescue are coupled functions of VHL

To learn more about potentially differential defects in the various pVHL mutants in terms of their function as catastrophe inhibitors and rescue factors, we next focused on shrinkage events, captured by reverse gaps between EB3 growth tracks. These covered 16–32% of the overall duration of multitrack trajectories (Fig. 4 C, horizontal axis). At the lower end of this range, RCC-4 cells producing the long form $pVHL_{30}$(wt) clustered with mutants that had wild-type behavior with respect to speed attenuation. These include the type 2B $pVHL_{30}$ mutants R167W and Y98N. At the intermediate level, RCC-4 cells producing the short form $pVHL_{19}$(wt), the type 2B mutant G114S, and the type 2C mutant L188V were clustered. Like $pVHL_{19}$(wt), these two mutants also displayed an intermediate increase in speed attenuation (Fig. 4 B). At the upper end, *VHL*-negative RCC-4 cells and the type 2A mutant $pVHL_{30}$(Y98H), which exhibited complete loss of function with respect to speed attenuation, as well as the type 2B mutant $pVHL_{30}$(R161P), which retained, unlike the other species within this cluster, speed attenuation function, were clustered. Interestingly, mutants

generally showed a tight positive correlation between the time spent in shrinkage and the probability of an MT to transition from a growth track into a reverse gap (Fig. 4 C). Thus, increased shrinkage time is associated with a higher rate of catastrophe events, suggesting that pVHL's functions as a catastrophe inhibitor and as a rescue factor are coupled. The exception to these rules was again the type 2B mutation $pVHL_{30}$(R161P). In contrast to the other type 2B mutations, this one is located in the Elongin C–binding domain of pVHL and therefore impaired the formation of a functional VHL–Elongin B–Elongin C–Cul2 complex (Ohh et al., 1999). MTs in cells expressing this mutant had a probability of switching from growth tracks into reverse gaps above the general trend line (Fig. 4 C). Consistent with an abnormally high catastrophe rate for $pVHL_{30}$(R161P), the fraction of EB3 growth tracks participating in multitrack trajectories dropped from a range of 65–72% to 48% (Table S5), suggesting that in cells expressing this mutant, a significant fraction of catastrophe events are terminal. Another mutant defective in Elongin C binding, $pVHL_{30}$(R167W) (Kishida et al., 1995), did not exhibit such a behavior. These analyses pinpoint that the two MT-regulatory functions of pVHL are differentially perturbed in disease-causing mutants and that current clinically defined genotype to phenotype associations are incomplete in distinguishing quantitative functional defects related to point mutations in different domains of the *VHL* gene product. Moreover, given that $pVHL_{30}$(R161P) and $pVHL_{30}$(R167W) mutant proteins are defective in targeting HIF-α subunits and are associated with a high risk of ccRCC, they suggest that certain *VHL* mutations that are linked to ccRCC development are defective in more than one distinct biochemical activity, which may profoundly influence the path of renal pathology in the setting of VHL disease.

Catastrophe inhibition and increased rescue are both promoted by pVHL-dependent reduction in GTP hydrolysis activity of MTs

To shed light on the biochemical mechanism by which VHL may affect MT polymerization dynamics, we asked whether pVHL would alter the rate of MT GTP hydrolysis in vitro. Indeed, in the presence of active $pVHL_{30}$, the rate of tubulin GTP hydrolysis was lower. This effect strictly depended on the ability of pVHL to bind MTs because the presence of $pVHL_{30}$(Δ95–123), a mutant lacking the MT interaction domain (Hergovich et al., 2003), failed to lower GTP hydrolysis (Fig. 5 A). The purity of the GST fusion proteins for the GTPase assay is documented in Fig. S5.

To extend this observation to an in vivo setting, we took advantage of an antibody that specifically recognizes GTP-tubulin. Using this antibody, it has been demonstrated that GTP-tubulin localizes not only at the MT tip but that remnants of GTP-tubulin can also be found along the entire MT lattice (Dimitrov et al., 2008). The study proposes that such remnants could serve as sites of rescue events for shrinking MTs. From these data, it follows that factors lowering the overall GTPase rate may increase the occurrence of GTP-tubulin caps at MT tips and thus reduce the frequency of catastrophe. At the same time, these factors may increase the occurrence of remnants along the lattice and thus enhance the frequency of rescue. Therefore, the coupled functions of pVHL as a catastrophe inhibitor and rescue factor could be explained by its effect on GTPase activity.

To test this directly, we determined the frequency and localization of GTP-tubulin by immunostaining in the presence and absence of $pVHL_{30}$ and of the various naturally occurring point mutants of $pVHL_{30}$. As shown in Fig. 5 B, when we analyzed the frequency of GTP-tubulin signals at the MT tips, we observed a significant reduction of signals in VHL-negative RCC-4 cells compared with those expressing wild-type $pVHL_{30}$. RCC-4 cells producing the short isoform $pVHL_{19}$ displayed an intermediate frequency of capped MT tips, but this is statistically insignificant because of the limited sampling. Most intriguingly, the frequency of GTP caps in cells expressing various disease-causing $pVHL_{30}$ mutants revealed a highly significant correlation with the shrinkage probabilities inferred by geometric grouping of plus end marker growth tracks (Fig. 5 C). First, these results confirm the accuracy of the grouping method in detecting shrinkage events. Second, they support the hypothesis that by interfering with tubulin GTPase activity, pVHL stabilizes MTs in part via reduction of catastrophe events.

Next, we determined whether pVHL would also influence the distances between GTP-tubulin remnants along the MT lattice in vivo, as it was suggested before that this distance is inversely proportional to the rescue frequency (Dimitrov et al., 2008). Indeed, in support of our conclusion from live cell imaging that pVHL is a rescue factor, we observed a reduction of the distance between GTP-tubulin remnants by ∼35% in $pVHL_{30}$-producing RCC-4 cells compared with control RCC-4 cells devoid of pVHL (Fig. 5 D), whereas expression of the short isoform $pVHL_{19}$ caused an intermediate reduction of the distance between GTP remnants along the MT lattice (Fig. 5 D). GTP remnant distances in RCC-4 cells expressing point mutants of $pVHL_{30}$ revealed excellent correlation between the distances between GTP-tubulin remnants along the MT lattice and the relative time in shrinkage (Fig. 5 E). Again, this validates the inference of rescue frequencies from grouped MT growth tracks. Two representative immunofluorescence pictures of RCC-4 control cells and RCC-4 cells producing wild-type $pVHL_{30}$ costained with antibodies against tubulin and GTP-tubulin exemplify these observations (Fig. 5 F). Because GTP remnant distances could only be measured on peripheral MTs, we additionally measured the relative intensity of the GTP-tubulin signal in perinuclear regions. This analysis also revealed significantly higher signal intensity in cells expressing $pVHL_{30}$ compared with VHL-negative cells (Fig. 5 G). Collectively, these results suggest a mechanism for pVHL's function to lower catastrophe rates and to enhance rescue rates: wild-type pVHL has the capacity to reduce the intrinsic GTPase activity of tubulin. Thereby, it increases the fraction of GTP-capped MT tips, which in turn inhibits MT catastrophe events. It also increases the frequency of GTP remnants along the MT lattice in vivo. Assuming that these remnants are preferred sites of MT rescue (Dimitrov et al., 2008), the shorter distances between remnants explain the higher probability for rescue. The reduction of GTPase activity is partially or fully impaired by point mutations in *VHL*, accompanied by a corresponding impairment of the pVHL gene product to act as a catastrophe inhibitor or rescue factor.

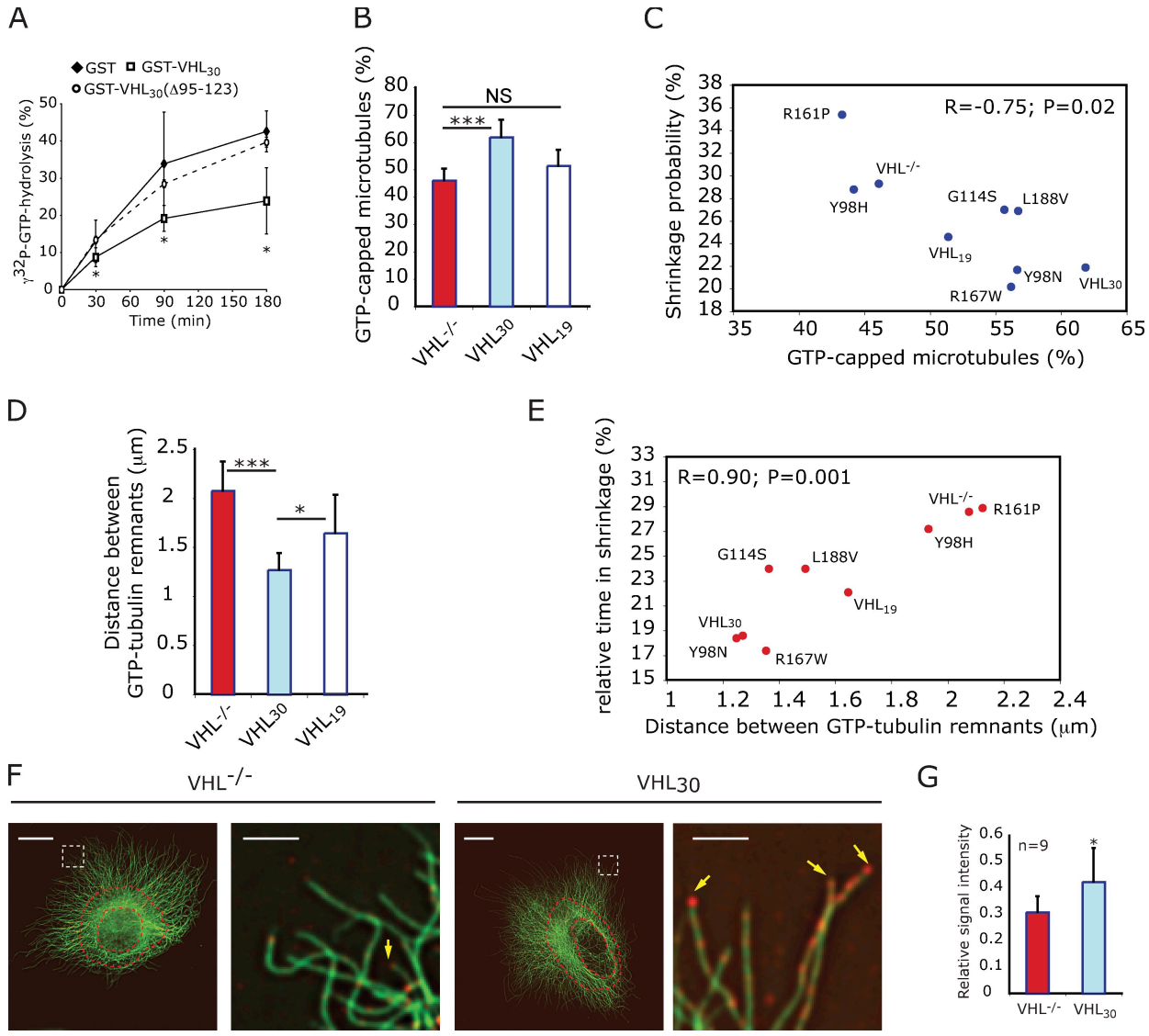

Figure 5. **pVHL reduces intrinsic GTPase activity of MTs, resulting in higher frequencies of GTP caps and GTP remnants along the MT lattice.** (A) MAP-purified tubulin was incubated with GST-VHL_{30}, GST-VHL_{30}(Δ95–123), or GST. Release of free ^{32}P from γ-[^{32}P]GTP was measured at the indicated time points. Error bars represent SD of $n = 9$ or $n = 3$ independent measurements for GST and GST-VHL_{30} or GST-VHL_{30}(Δ95–123), respectively (GST vs. GST-VHL_{30}(Δ95–123), NS; *, P = 0.04 and 0.01 [60 min]; *, P = 0.003 and 0.0007 [90 min]; *, P = 7×10^{-5} and 0.01 [180 min]; Student's *t* test [GST vs. GST-VHL_{30} and GST-VHL_{30}(Δ95–123) vs. GST-VHL_{30}]). (B) Frequency of GTP-capped MTs in RCC-4 cells expressing no VHL ($VHL^{-/-}$), wild-type long form (VHL_{30}), or wild-type short form (VHL_{19}). Mean ± SD is shown (***, P = 3.3×10^{-7}). (C) Scatter plot of shrinkage probability (see legend for Fig. 4 C) to GTP cap frequency (percentage of GTP-capped MTs) in RCC-4 cells expressing various naturally occurring VHL point mutants (Fig. 4 A; mean of $n = 12$ cells from three independent stainings, a total of >250 measurements per condition; Spearman correlation). (D) Distance between GTP-tubulin remnants in RCC-4 cells expressing no VHL ($VHL^{-/-}$), wild-type long form (VHL_{30}), or wild-type short form (VHL_{19}; mean ± SD of $n = 12$ cells from three independent stainings; *, P = 0.03; ***, P = 3.4×10^{-6}). (E) Scatter plot of relative time in shrinkage (see legend for Fig. 4 C) to GTP remnant distance in RCC-4 cells expressing various naturally occurring VHL point mutants (Fig. 4 A; mean of $n = 12$ cells from three independent stainings, a total of >500 measurements per condition; Spearman correlation). (F) Immunofluorescence costaining with anti–α-tubulin (green) and anti–GTP-tubulin (red) of RCC-4 cells reconstituted with VHL_{30} or the empty vector as control ($VHL^{-/-}$). Zoomed areas (right) are indicated by a dashed square in the panels to the left. Yellow arrows show GTP-capped MTs. Red lines indicate perinuclear area where the GTP remnant signal was measured. Bars: (left) 10 μm; (right) 2 μm. (G) GTP remnant signal intensity relative to tubulin intensity of RCC-4 cells reconstituted with VHL_{30} or the empty vector as control ($VHL^{-/-}$; mean ± SD of $n = 9$ cells from three independent stainings; *, P < 0.05; Student's *t* test).

Discussion

Based on our results, we propose that pVHL functions as a MAP with dedicated MT-stabilizing function: (a) it dampens addition of tubulin dimers in growth, thus avoiding depletion of the pool of free tubulin dimers; (b) it dampens the removal of tubulin dimers during shrinkage, thus avoiding rapid, catastrophic disassembly of parts of the MT network; (c) it limits the switches from well-controlled growth to well-controlled shrinkage; and (d) if the switch occurs, it enhances the probability for returning into a growth state.

A mechanistic explanation for pVHL's dual roles as a catastrophe inhibitor and rescue factor is provided by its inhibitory action on GTPase activity of tubulin in vitro, which translates into a measurable higher frequency of GTP-tubulin remnants along the MT lattice and on MT plus ends in vivo. Although we

cannot formally exclude the possibility that regulation of GTPase activity by pVHL is also implicated in pVHL-mediated control of MT turnover, MT stability and turnover are differentially affected by naturally occurring pVHL mutants, implying that they represent separable activities of pVHL.

We also found that different *VHL* disease mutants were associated with profound differences in their ability to regulate various parameters of MT dynamic instability. From clinical work (Crossey et al., 1994; Chen et al., 1995), genotype–phenotype correlations have emerged with respect to the organ-specific risk of tumor development in VHL disease. All *VHL* mutations linked to classical VHL disease have been found to compromise pVHL's HIF-α regulatory function. However, some missense mutations result in a low risk of kidney cancer (type 2A VHL disease), whereas others result in a high risk (type 2B VHL disease). Therefore, it is still not fully understood why type 2A and type 2B *VHL* mutations are associated with markedly different risks of developing renal carcinoma. Quantitative differences between the ability of these various pVHL mutants to target HIF-α may provide part of the explanation (Li et al., 2007). Our ability to quantitatively assess various parameters of MT dynamic instability allowed us to provide potential explanations for the different phenotypes. We found that type 2A pVHL mutants are compromised in their ability to lower the speed of tubulin turnover both at growing and shrinking MT ends, as well as in inhibiting catastrophe and enhancing rescue events. Thus, these missense mutations behave with respect to MT regulation equivalent to *VHL*-negative cells, except that type 2A *VHL* disease mutations are less defective in HIF-α control and are not associated with a high risk of developing renal carcinoma. However, type 2A *VHL* disease is characterized by renal cyst formation, implying an explicit link between the disruption of multiple parameters of MT dynamic instability and the development of a hallmark feature of the VHL cancer syndrome. Based on these observations, we propose a model in which cyst formation in type 2A VHL disease occurs as the result of disruption of MT regulation by pVHL in the absence of any quantitative differences in HIF-α regulation.

Our analysis of different type 2B pVHL mutants, which have all been previously shown to be defective in HIF degradation (Li et al., 2007), revealed striking differences with respect to the regulation of MT dynamic instability parameters. Specifically, the pVHL mutant R161P displays defects in MT stabilization but not turnover function. In contrast, the mutant G114S is disrupted in MT turnover but not stabilization function. Moreover, the pVHL mutants, R167W and Y98N, behaved like wild-type pVHL with respect to MT regulation. Thus, distinct *VHL* mutations associated with type 2B VHL disease commonly compromise the ability of pVHL to regulate HIF but generate different patterns of MT dynamic instability. Given these observations, the fact that ccRCC is a common clinical endpoint of all type 2B *VHL* disease mutations (Kondo et al., 2002; Gallou et al., 2004) and that these mutations are all defective in HIF-α degradation, it is conceivable that the specific pattern of altered MT dynamic instability produced by various type 2B *VHL* disease mutations characterize distinct subgroups of type 2B *VHL* disease. It is intriguing to reason that specific patterns of MT dynamic instability influence the path of disease in the setting of the *VHL* cancer syndrome. For example, ccRCC development in the context of the type 2B pVHL mutants R161P and G114S may be cyst dependent and in the case of pVHL mutants R167W and Y98N cyst independent. Such a new subclassification of type 2B VHL disease that is based on patterns of altered MT dynamic instability may ultimately also profoundly impact treatment of VHL-associated cancers. Clearly, future whole-animal studies using knockin mice with the corresponding mutants will be required to test these predictions from a single-cell assay of MT dynamics.

Finally, these experiments demonstrate that the sensitivity of computer-based live cell readouts is becoming capable of identifying subtle implications of individual protein domains on cell function in vivo. The practical simplicity of our assay can bring high-content in situ live cell measurements of MT dynamics into the realm of high-resolution screening applications. This approach can significantly expand our knowledge on the physiology of MTs and their roles in disease as well as allow the identification of new anticancer agents that target distinct aspects of MT dynamics.

Materials and methods

Cloning of vectors

For the generation of retroviral VHL expression plasmids pCMV(R)-neo and pBabe-neo, the fragments were subcloned by digestion of corresponding pcDNA3-HA-VHL vectors that have been described previously (Hergovich et al., 2003) using BamHI–XhoI fragments for pCMV(R)-neo and BamHI–EcoRI fragments for pBabe-neo. The BamHI–Xho1 fragments were subsequently blunted using mung bean nuclease and ligated into pCMV(R)-neo vector linearized with EcoRV. The BamHI–EcoRI fragments were ligated into pBabe-neo vector linearized with BamHI–EcoRI.

The pLMP-EB3GFP vector was cloned by PCR amplification of the EB3GFP fragment from the vector pGFP-N1-EB3 (gift from N. Galjart, Erasmus Medical Center, Rotterdam, Netherlands) using an N-terminal primer introducing a PciI site (5′-CGTGACATGTATGGCAGTGAATGTGTACTCTACGTCAGTCACC-3′) and a C-terminal primer introducing a SalI site (5′-GTACCGTCGACTTACTTGTACAGCTCGTCCATGC-3′). The PCR fragment was purified and digested with PciI and SalI and ligated into pLMP (gift from S. Lowe, Cold Spring Harbor Laboratory, Cold Spring Harbor, NY) linearized with NcoI and SalI. The cloning of the *VHL*-targeting (*shVHL*) and the nonsilencing (ns-control) shRNAmir into pLMP-EB3GFP have been described previously (Hergovich et al., 2006). pCMV-NEO-ZEO was cloned as described previously (Frew et al., 2008). The cloning of the *VHL*-targeting and the ns-control shRNAmir into pCMV-NEO-ZEO was performed as for the pLMP-EB3GFP vector. Transient expression of pGFP-N1-EB3 and pGFP-C1-CLIP170 in RPE-1 cells (gift from F. Perez, Institut Curie, Paris, France) was performed with Fugene 6 (Roche) according to the manufacturer's manual.

Generation and maintenance of cell lines

RCC-4 cells (provided by P. Maxwell, University College London, London, England, UK) were infected with retroviral vectors pCMV(R)-neo or pBabe-neo to express the different VHL mutants as described previously (Thoma et al., 2007). To express EB3-GFP, RCC-4 cells expressing VHL mutant proteins were super-infected with the retroviral vector pLMP-EB3GFP as described previously (Thoma et al., 2007). RPE-1 cells were infected with the retroviral vector pLMP-shRNAmir-EB3GFP expressing additionally an ns-control or a *VHL*-targeting shRNAmir as described previously (Thoma et al., 2007). RCC-4 cells were cultured in DME 10% FCS, RPE-1 cells were cultured in DME/F12 10% FCS. In RPE-1 cells expressing either GFP-CLIP170 or GFP–α-tubulin, pVHL was depleted using stable lentiviral transfection (pCMV-NEO-ZEO) of shRNAmir against VHL (*shVHL*) and a nonsilencing control (ns-control) as described previously (Frew et al., 2008).

Western blots

Cells were lysed in TNN buffer (25 mM Tris-HCl, pH 7.2, 150 mM Na chloride, 10% glycerol, 1% NP-40, 10 mM Na fluoride, 1 mM Na_3VO_4, 1 mM PMSF, 1 mM dithiothreitol, and 10 µg/ml aprotinin) for protein extraction.

Proteins were run on 10–12% acrylamide gels, transferred to nitrocellulose membranes, and visualized by immunoblotting with following antibodies: rabbit anti–human $pVHL^{CT}$ and rabbit anti–human $pVHL^{NT}$ (1:500 dilution; Hergovich et al., 2003), anti-CDK-2 (1:1,000; Santa Cruz Biotechnology, Inc.), and anti–α-tubulin YL1/2 (1:3,000; Harlan Laboratories).

Live cell imaging of EB3-GFP and GFP-CLIP170–expressing cells

Cells were distributed 24 h before video acquisition in 6-well plates containing round coverslips (diameter 24 mm; #1.5) and cultured to ∼50% confluency in the appropriate medium containing 25 mM Hepes. Cells on round coverslips were transferred to a homemade holding device, and 600 µl of the appropriate medium was added. Videos were acquired with a microscope (IX70 Delta Vision Spectris; Olympus), temperature-controlled at 37°C, using a 60× NA 1.4 differential interference contrast (DIC) oil Plan-Apochromat objective and a camera (CoolSNAP HQ; Roper Industries) with an exposure time of 100 ms and a frame rate of 2 Hz. Acquisition software used was SoftWoRx version 3.3.4 (Applied Precision). For nocodazole experiments, a first video was acquired in 300 µl of normal growth medium, and then 300 µl of growth medium containing 80 nM nocodazole was added, leading to a final concentration of 40 nM, and a video at 20, 120, and 360 s after nocodazole addition was acquired from the very same position.

Live cell imaging of GFP-tubulin and manual tracking

RPE-1 cells stably expressing GFP–α-tubulin (Rosa et al., 2006) were cultured and prepared for live cell imaging the same way as RPE-1 EB3-GFP–expressing cells. Videos were acquired as EB3-GFP videos except using a 100× NA 1.4 DIC oil Plan-Apochromat objective with an exposure time of 200 ms and a frame rate of 0.5 Hz. From these acquired videos, MTs were manually tracked using SoftWoRx version 3.3.4. Intervals with a velocity <0.1 µm/s were defined as a pause events. Videos were acquired in two independent sessions, and manual tracking was performed on 20 MTs in at least three different cells per condition from each session.

Immunofluorescence and measurement of GTP-tubulin remnants

Immunofluorescence staining of tubulin and GSK-3β was performed as previously described (Thoma et al., 2007) using monoclonal GSK-3β antibody (1:200; BD) and a polyclonal antibody recognizing α-tubulin (1:400; Abcam) and using a confocal microscope (SP2-AOBS; Leica) with a 63× NA 1.4 oil HCX Plan-Apochromat objective. Signal intensities were measured for each channel using ImageJ software (National Institutes of Health).

For GTP-tubulin staining, RCC-4 cells were distributed on glass coverslips and processed for costaining with a monoclonal antibody recognizing GTP-tubulin (hMB11; 1:200; Dimitrov et al., 2008) and a polyclonal antibody recognizing α-tubulin (1:400; Abcam) as described previously (Dimitrov et al., 2008). Stacks from randomly chosen cells were acquired with an IX70 Delta Vision Spectris microscope using a 60× NA 1.4 DIC Oil Plan-Apochromat objective. After deconvolution using SoftWoRx version 5.3.1, >20 distances between GTP remnants were measured per cell from peripheral MTs, where remnants were clearly resolved and assigned to the same MT, using SoftWoRx version 5.3.1. Remnant density in the perinuclear cell region was determined by the area density of fluorescence accumulated in a manually selected region using ImageJ software.

In vitro MT GTPase assay

Cloning and purification of GST, GST-VHL_{30}, and GST-$VHL_{30,\Delta 95–123}$ fusion proteins has been described previously (Hergovich et al., 2006). EasyRad phosphate assay biochem kit (Cytoskeleton, Inc.) was used to measure the release of ^{32}P from γ-[^{32}P]GTP (Hartmann Analytic) from MAP-rich tubulin (Cytoskeleton, Inc.) supplemented with GST fusion proteins. A reaction mix was prepared containing 1 mg ml^{-1} MAP-rich tubulin, 10 µM GTP, 20 nM γ-[^{32}P]GTP, and 0.5 µM GST fusion protein in 100 µl reaction buffer (EasyRad phosphate assay) and incubated at 37°C. Aliquots of 10 µl were taken at the indicated time points, put into 400 µl of separator solution (EasyRad phosphate assay), and put on ice. An aliquot to measure the background value was taken 10 s after incubation at 37°C and put into 400 µl of separator solution, and an aliquot was added at the end to 400 µl double distilled H_2O to measure total activity. Collected samples were centrifuged at 14,000 rpm for 10 min, and 200 µl of the supernatant was measured in a scintillation counter (LS 6500; Beckman Coulter).

Image analysis

All image analysis programs for detection of individual EB3 features, feature tracking, clustering of growth tracks, parsing of MT trajectories for extraction of MT dynamics, statistical analysis of MT dynamics, and graphical representation of the results were developed in MATLAB (MathWorks) and C++. The algorithms for each of the steps are described in detail in Matov et al. (2010). The same paper documents the validation of each of the steps in reference to simultaneously acquired time-lapse sequences of mCherry-tubulin–labeled MTs and GFP-EB1 and in reference to well-characterized small molecule inhibitors of MT polymerization dynamics. Together with the comparison of hand measurements and automated image analysis of the effects of silencing pVHL in RPE-1 cells, and with the agreement between the conclusions drawn from the distribution of GTP remnants and the image analysis provided in this study, the tests conducted in Matov et al. (2010) established the validity of the analysis of MT regulatory functions of pVHL based on live cell images of a plus end marker.

In brief, EB3 comet detection is accomplished by band-pass filtering, which enhances image features of the expected size of an EB3 comet while it oppresses higher-frequency noise and lower-frequency structures representing larger aggregates of fluorescent protein. Importantly, the algorithm is robust against variations in comet lengths, both within videos and between videos. Within videos, EB3 comets differ in length mainly because of the variable speed of MT growth. Between videos, EB3 comets differ in length because of variable EGFP-EB3 expression levels. The feature detector delivers not only the position of each comet in a frame but also the eccentricity and orientation of the comets. The latter is used as a directional cue in the subsequent tracking of comets from one frame to the next.

Frame to frame tracking is performed by solving a linear assignment problem (LAP; Schrijver, 2003), which identifies the globally optimal positional correspondences between the set of comets measured in frame t and the set of comets measured in frame $t + 1$. To render the assignment robust despite the substantial frame to frame displacements of comets, the comet positions in frame t are first projected into frame $t + 1$ using a Kalman filter (Jaqaman et al., 2008). Therefore, the assignment has to account only for the differences between projection and actual comet position at time point $t + 1$. Growth tracks with a lifetime of more than four frames are eliminated from further analysis.

To cluster collinear growth tracks that likely belong to the same MT, we again solve a LAP, here between the endpoints of terminating tracks and the start points of newly initiated tracks. A pairing between a track termination and a track initiation is considered only if these two events are separated by less than 30 frames; i.e., forward and backward gaps of a maximum of 15 s are allowed. Furthermore, the track initiation has to fall within either one of two cone-shaped, geometrical search regions (Fig. S3). The choice of the forward cone with an opening half-angle of 60° is motivated by the observation that during pauses or out of focus movements, MTs sometimes undergo significant lateral displacements and directional changes, especially at the cell periphery. The longer the gap duration, the larger is the probability for a lateral step and directional change. In contrast, the backward cone has an opening half-angle of 10° only, motivated by the observation that MT rescues generally follow the growth track before the catastrophe. The search space for possible pairings between growth track terminations and growth track initiations is also limited by a distance cutoff, which depends on the gap duration and the maximal anticipated speeds of MT growth and shrinkage. The latter are calculated from the initial speed distribution of the growth tracks and thus are automatically determined by the software. All growth track pairings that pass these criteria participate then in the LAP. By construction, this assignment is spatially and temporally global, which warrants a high level of robustness. Competing pairings are weighed against one another via a cost function that prefers collinear track parings with a short gap distance (Matov et al., 2010). During the validation, it was noted that the selection of candidate track pairings tends to exclude a significant number of true pairings from the LAP. As a result, the analysis generates a relatively high fraction of false negatives; however, because of strict selection criteria, the number of false positives is low. Given the large number of trajectories harvested from these videos, the high number of false negatives is uncritical as long as they do not lead to a systematic exclusion of certain forward and background gap events. In Matov et al. (2010), it is shown that with the parameter settings described in this study, computer-generated distributions of growth and shrinkage speeds as well as pause frequencies and duration are statistically identical to the same distributions extracted from manual tracking of α-tubulin–labeled MTs.

Merging of data from multiple videos per condition

For each condition, at least 15 videos containing one or two cells were acquired. Before merging the data for further statistical analysis, we determined the video to video variation in the distributions of speeds and durations of growth, pause, and shrinkage events using the Kolmogorov-Smirnov test. Distributions were subsampled to 400 values to avoid hypersensitivity of the Kolmogorov-Smirnov statistics. Videos passing the

consistency test were included in the final datasets. The number of mutually consistent videos per dataset is documented in Tables S2–S5.

Statistical analyses of parameters of MT dynamics

Statistical comparison of MT dynamics between different conditions was accomplished in two steps for the distributions of growth, pause, and shrinkage speed distributions. First, we examined whether the different conditions would profoundly change the distribution, which would indicate an entirely different state of MT regulation between conditions. To test this possibility, we aligned the distributions of compared conditions at their respective mean value and then applied the nonparametric Kolmogorov-Smirnov test to determine whether the two distributions are identical. The distributions were randomly subsampled to 400 values. The subsampling was repeated 200 times, and the final p-values were derived by averaging.

In a second step, we compared the shifts in parameter mean values between different conditions. To achieve this, we calculated the mean of a specific parameter, e.g., growth speed, per video. Then we tested normality of the distribution of the means and applied the Student's *t* test to define the significance of parameter changes between conditions (mean ± SEM of cell to cell variation). This test assumes that the cell to cell variation is the single biggest source of variation in the mean value of a condition.

For the comparison of manually tracked parameters of MT dynamics between nonsilenced and VHL-silenced RPE-1 cells, the dataset was not sufficiently large enough to follow the aforementioned test procedures. Instead, we used the permutation *t* test (Hesterberg et al., 2005), which compares the bootstrapped distributions of a parameter in condition 1 versus condition 2. This test does not make any assumption about the characteristic of the tested distribution and thus is appropriate for application to the distributions of growth and shrinkage speeds and of growth, pause, and shrinkage times, which are far from being normally distributed.

Online supplemental material

Fig. S1 shows manual GFP-tubulin tracking in RPE-1 cells depleted for VHL and comparison of automated tracking of EB3-GFP and GFP-CLIP170 as markers of MT growth. Fig. S2 shows colocalization of pVHL and EB3 comets in RPE-1 cells. Fig. S3 schematically explains the grouping of MT growth tracks. Fig. S4 provides additional analysis of naturally occurring VHL point mutants. Fig. S5 shows the purification of GST fusion proteins for the GTPase assay. Video 1 shows detection of EB3-GFP comets in RPE-1 cells. Video 2 illustrates the large number and high density of tracked EB3-GFP comets captured for a single RCC-4 cell in a typical time-lapse video. Videos 3 and 4 illustrate in an overview and zoomed version the comet tracking and growth track grouping that allow inference of parameters of MT dynamics in RPE-1 cells. Video 5 compares the number of EB3-GFP comets detected after nocodazole perturbation in a cell without and with active VHL. Tables S1–S5 provide all of the parameters of MT dynamics extracted by tracking of GTP-tubulin (Table S1) and EB3-GFP (Tables S2–S5). Online supplemental material is available at http://www.jcb.org/cgi/content/full/jcb.201006059/DC1.

We thank all members of our laboratories for helpful discussions. We are grateful to N. Galjart, F. Perez, and P. Maxwell for their gifts of reagents and the Light Microscopy Centre ETH Zurich for help with microscopy.

W. Krek is supported by a grant from the Swiss National Science Foundation. G. Danuser is supported by National Institutes of Health grant U01 GM67230.

Submitted: 10 June 2010
Accepted: 19 August 2010

References

Chen, F., T. Kishida, M. Yao, T. Hustad, D. Glavac, M. Dean, J.R. Gnarra, M.L. Orcutt, F.M. Duh, G. Glenn, et al. 1995. Germline mutations in the von Hippel-Lindau disease tumor suppressor gene: correlations with phenotype. *Hum. Mutat.* 5:66–75. doi:10.1002/humu.1380050109

Crossey, P.A., F.M. Richards, K. Foster, J.S. Green, A. Prowse, F. Latif, M.I. Lerman, B. Zbar, N.A. Affara, M.A. Ferguson-Smith, et al. 1994. Identification of intragenic mutations in the von Hippel-Lindau disease tumour suppressor gene and correlation with disease phenotype. *Hum. Mol. Genet.* 3:1303–1308. doi:10.1093/hmg/3.8.1303

Dimitrov, A., M. Quesnoit, S. Moutel, I. Cantaloube, C. Poüs, and F. Perez. 2008. Detection of GTP-tubulin conformation in vivo reveals a role for GTP remnants in microtubule rescues. *Science*. 322:1353–1356. doi:10.1126/science.1165401

Frew, I.J., and W. Krek. 2008. pVHL: a multipurpose adaptor protein. *Sci. Signal.* 1:pe30. doi:10.1126/scisignal.124pe30

Frew, I.J., C.R. Thoma, S. Georgiev, A. Minola, M. Hitz, M. Montani, H. Moch, and W. Krek. 2008. pVHL and PTEN tumour suppressor proteins cooperatively suppress kidney cyst formation. *EMBO J.* 27:1747–1757. doi:10.1038/emboj.2008.96

Gallou, C., D. Chauveau, S. Richard, D. Joly, S. Giraud, S. Olschwang, N. Martin, C. Saquet, Y. Chrétien, A. Méjean, et al. 2004. Genotype-phenotype correlation in von Hippel-Lindau families with renal lesions. *Hum. Mutat.* 24:215–224. doi:10.1002/humu.20082

Hergovich, A., J. Lisztwan, R. Barry, P. Ballschmieter, and W. Krek. 2003. Regulation of microtubule stability by the von Hippel-Lindau tumour suppressor protein pVHL. *Nat. Cell Biol.* 5:64–70. doi:10.1038/ncb899

Hergovich, A., J. Lisztwan, C.R. Thoma, C. Wirbelauer, R.E. Barry, and W. Krek. 2006. Priming-dependent phosphorylation and regulation of the tumor suppressor pVHL by glycogen synthase kinase 3. *Mol. Cell. Biol.* 26:5784–5796. doi:10.1128/MCB.00232-06

Hesterberg, T.C., D.S. Moore, S. Monaghan, A. Clipson, and R. Epstein. 2005. Bootstrap methods and permutation tests. *In* Introduction to the Practice of Statistics. Fifth edition. D.S. Moore and G.P. McCabe, editors. W.H. Freeman and Co., New York. 14.1–14.70.

Hoffman, M.A., M. Ohh, H. Yang, J.M. Klco, M. Ivan, and W.G. Kaelin Jr. 2001. von Hippel-Lindau protein mutants linked to type 2C VHL disease preserve the ability to downregulate HIF. *Hum. Mol. Genet.* 10:1019–1027. doi:10.1093/hmg/10.10.1019

Iliopoulos, O., M. Ohh, and W.G. Kaelin Jr. 1998. pVHL19 is a biologically active product of the von Hippel-Lindau gene arising from internal translation initiation. *Proc. Natl. Acad. Sci. USA*. 95:11661–11666. doi:10.1073/pnas.95.20.11661

Jaqaman, K., J.F. Dorn, G.S. Jelson, J.D. Tytell, P.K. Sorger, and G. Danuser. 2006. Comparative autoregressive moving average analysis of kinetochore microtubule dynamics in yeast. *Biophys. J.* 91:2312–2325. doi:10.1529/biophysj.106.080333

Jaqaman, K., D. Loerke, M. Mettlen, H. Kuwata, S. Grinstein, S.L. Schmid, and G. Danuser. 2008. Robust single-particle tracking in live-cell time-lapse sequences. *Nat. Methods*. 5:695–702. doi:10.1038/nmeth.1237

Kaelin, W.G. Jr. 2008. The von Hippel-Lindau tumour suppressor protein: O2 sensing and cancer. *Nat. Rev. Cancer*. 8:865–873. doi:10.1038/nrc2502

Kaelin, W.G. Jr., and P.J. Ratcliffe. 2008. Oxygen sensing by metazoans: the central role of the HIF hydroxylase pathway. *Mol. Cell*. 30:393–402. doi:10.1016/j.molcel.2008.04.009

Keller, P.J., F. Pampaloni, and E.H. Stelzer. 2007. Three-dimensional preparation and imaging reveal intrinsic microtubule properties. *Nat. Methods*. 4:843–846. doi:10.1038/nmeth1087

Kishida, T., T.M. Stackhouse, F. Chen, M.I. Lerman, and B. Zbar. 1995. Cellular proteins that bind the von Hippel-Lindau disease gene product: mapping of binding domains and the effect of missense mutations. *Cancer Res.* 55:4544–4548.

Knauth, K., C. Bex, P. Jemth, and A. Buchberger. 2006. Renal cell carcinoma risk in type 2 von Hippel-Lindau disease correlates with defects in pVHL stability and HIF-1alpha interactions. *Oncogene*. 25:370–377.

Knauth, K., E. Cartwright, S. Freund, M. Bycroft, and A. Buchberger. 2009. VHL mutations linked to type 2C von Hippel-Lindau disease cause extensive structural perturbations in pVHL. *J. Biol. Chem.* 284:10514–10522. doi:10.1074/jbc.M809056200

Kondo, K., M. Yao, M. Yoshida, T. Kishida, T. Shuin, T. Miura, M. Moriyama, K. Kobayashi, N. Sakai, S. Kaneko, et al. 2002. Comprehensive mutational analysis of the VHL gene in sporadic renal cell carcinoma: relationship to clinicopathological parameters. *Genes Chromosomes Cancer*. 34:58–68. doi:10.1002/gcc.10054

Li, L., L. Zhang, X. Zhang, Q. Yan, Y.A. Minamishima, A.F. Olumi, M. Mao, S. Bartz, and W.G. Kaelin Jr. 2007. Hypoxia-inducible factor linked to differential kidney cancer risk seen with type 2A and type 2B VHL mutations. *Mol. Cell. Biol.* 27:5381–5392. doi:10.1128/MCB.00282-07

Matov, A., K. Applegate, P. Kumar, C.R. Thoma, W. Krek, G. Danuser, and T. Wittmann. 2010. Analysis of microtubule dynamic instability using a plus-end growth marker. *Nat. Methods*. 7:761–768. doi:10.1038/nmeth.1493

Mitchison, T., and M. Kirschner. 1984. Dynamic instability of microtubule growth. *Nature*. 312:237–242. doi:10.1038/312237a0

Ohh, M., Y. Takagi, T. Aso, C.E. Stebbins, N.P. Pavletich, B. Zbar, R.C. Conaway, J.W. Conaway, and W.G.J. Kaelin Jr. 1999. Synthetic peptides define critical contacts between elongin C, elongin B, and the von Hippel-Lindau protein. *J. Clin. Invest.* 104:1583–1591. doi:10.1172/JCI8161

Perez, F., G.S. Diamantopoulos, R. Stalder, and T.E. Kreis. 1999. CLIP-170 highlights growing microtubule ends in vivo. *Cell*. 96:517–527. doi:10.1016/S0092-8674(00)80656-X

Rosa, J., P. Canovas, A. Islam, D.C. Altieri, and S.J. Doxsey. 2006. Survivin modulates microtubule dynamics and nucleation throughout the cell cycle. *Mol. Biol. Cell*. 17:1483–1493. doi:10.1091/mbc.E05-08-0723

Schek, H.T. III, M.K. Gardner, J. Cheng, D.J. Odde, and A.J. Hunt. 2007. Microtubule assembly dynamics at the nanoscale. *Curr. Biol.* 17:1445–1455. doi:10.1016/j.cub.2007.07.011

Schermer, B., C. Ghenoiu, M. Bartram, R.U. Müller, F. Kotsis, M. Höhne, W. Kühn, M. Rapka, R. Nitschke, H. Zentgraf, et al. 2006. The von Hippel-Lindau tumor suppressor protein controls ciliogenesis by orienting microtubule growth. *J. Cell Biol.* 175:547–554. doi:10.1083/jcb.200605092

Schrijver, A. 2003. Combinatorial Optimization. Springer, Heidelberg. 1,800 pp.

Stepanova, T., J. Slemmer, C.C. Hoogenraad, G. Lansbergen, B. Dortland, C.I. De Zeeuw, F. Grosveld, G. van Cappellen, A. Akhmanova, and N. Galjart. 2003. Visualization of microtubule growth in cultured neurons via the use of EB3-GFP (end-binding protein 3-green fluorescent protein). *J. Neurosci.* 23:2655–2664.

Thoma, C.R., I.J. Frew, C.R. Hoerner, M. Montani, H. Moch, and W. Krek. 2007. pVHL and GSK3beta are components of a primary cilium-maintenance signalling network. *Nat. Cell Biol.* 9:588–595. doi:10.1038/ncb1579

Thoma, C.R., A. Toso, K.L. Gutbrodt, S.P. Reggi, I.J. Frew, P. Schraml, A. Hergovich, H. Moch, P. Meraldi, and W. Krek. 2009. VHL loss causes spindle misorientation and chromosome instability. *Nat. Cell Biol.* 11:994–1001. doi:10.1038/ncb1912

Vasquez, R.J., B. Howell, A.M.C. Yvon, P. Wadsworth, and L. Cassimeris. 1997. Nanomolar concentrations of nocodazole alter microtubule dynamic instability in vivo and in vitro. *Mol. Biol. Cell*. 8:973–985.

Weisenberg, R.C., W.J. Deery, and P.J. Dickinson. 1976. Tubulin-nucleotide interactions during the polymerization and depolymerization of microtubules. *Biochemistry*. 15:4248–4254. doi:10.1021/bi00664a018